ACS APPLIED MATERIALS & INTERFACES

Research Article

www.acsami.org

# Improving the Efficiency of Hematite Nanorods for Photoelectrochemical Water Splitting by Doping with Manganese

Gurudayal,[†] Sing Yang Chiam,[‡] Mulmudi Hemant Kumar,[†] Prince Saurabh Bassi,[†] Hwee Leng Seng,[‡] James Barber,*[,†,§,∥] and Lydia Helena Wong*[,†]

[†]Solar Fuels Lab, School of Materials Science and Engineering, Nanyang Technological University, 639798, Singapore

[‡]Institute of Materials Research and Engineering (IMRE), Agency of Science, Technology, and Research (A*Star), 3 Research Link, 117602, Singapore

[§]Applied Science and Technology Department, BioSolar Lab, Politecnico di Torino, Viale T. Michel 5, 15121 Alessandria, Italy

[∥]Department of Life Sciences, Imperial College London, London SW7 2AZ, United Kingdom

Supporting Information

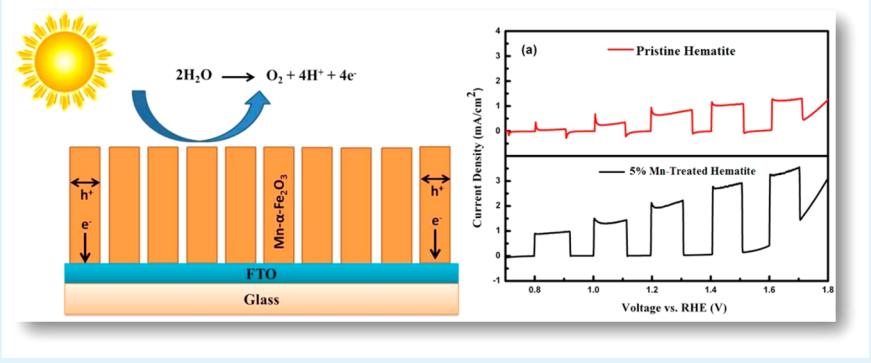


**ABSTRACT:** Here, we report a significant improvement of the photoelectrochemical (PEC) properties of hematite ($\alpha$-$Fe_2O_3$) to oxidize water by doping with manganese. Hematite nanorods were grown on a fluorine-treated tin oxide (FTO) substrate by a hydrothermal method in the presence on Mn. Systematic physical analyses were performed to investigate the presence of Mn in the samples. $Fe_2O_3$ nanorods with 5 mol % Mn treatment showed a photocurrent density of 1.6 mA $cm^{-2}$ (75% higher than that of pristine $Fe_2O_3$) at 1.23 V versus RHE and a plateau photocurrent density of 3.2 mA $cm^{-2}$ at 1.8 V versus RHE in a 1 M NaOH electrolyte solution (pH 13.6). We attribute the increase in the photocurrent density, and thus in the oxygen evolving capacity, to the increased donor density resulting from Mn doping of the $Fe_2O_3$ nanorods, as confirmed by Mott–Schottky measurement, as well as the suppression of electron–hole recombination and enhancement in hole transport, as detected by chronoamperometry measurements.

**KEYWORDS:** *hematite, photoelectrochemistry, water splitting, artificial photosynthesis, $Fe_2O_3$, Mott–Schottky*

## INTRODUCTION

Photoelectrochemistry (PEC) offers a unique and efficient way to convert solar energy into chemical energy.[1−3] Hematite ($\alpha$-$Fe_2O_3$) has emerged as one of the most promising candidates for solar-driven water splitting because of its favorable band gap energy (2.0 to 2.2 eV), good stability in aqueous solutions, nontoxicity, abundance, and economic viability.[4,5] Hematite has been theoretically predicted to achieve a water oxidation efficiency of 12.4%.[6] However, the reported efficiencies of hematite are lower than this predicted value because of the short lifetime of its photogenerated charge carriers (<10 ps), short hole diffusion length (2−4 nm), slow oxygen evolution reaction kinetics, and non-ideal conduction band position to reduce water.[2,7−10] Because of the latter, there is a requirement for an external applied bias (onset potential) for hydrogen production.[2,7−10]

To address the above-mentioned drawbacks, nanostructuring, surface modification, and doping of hematite have been explored to improve its electronic and optical properties.[11−14] Morphological control of these nanostructures for improved performance can be accomplished by employing various synthesis routes such as solution-based colloidal methods,[15,16] electrodeposition,[17] spray pyrolysis,[18] and atmospheric pressure chemical vapor deposition (APCVD).[19] Improvements in the conversion efficiencies of Si-treated hematite have been attributed to the dendritic nanostructure, which minimizes the distance that photogenerated holes have to travel to reach the $Fe_2O_3$–electrolyte interface.[20] Similarly, nanowire or

Received: February 2, 2014
Accepted: March 25, 2014
Published: March 26, 2014

nanorod arrays are promising candidates for achieving large photocurrents because the diameters can be controlled so that they are in the range of the hole diffusion length.[21−23] There are a number of methods to fabricate hematite nanorods on conducting substrates, including thermal oxidation of iron foil,[24] the use of an anodic aluminium oxide (AAO) template,[25] and precipitation of $Fe^{3+}$ from aqueous solution under hydrothermal conditions.[11,13] Among these methods, hydrothermal precipitation of $Fe^{3+}$ is the most simple and effective method to produce a large and uniform array of nanorods on conductive substrates. In our previous study,[26] hematite nanorod arrays were successfully grown on conducting fluorine-treated tin oxide (FTO) substrates by using urea as a pH-regulating agent. In comparison with other nanostructures, the nanorods that we grew showed better energy conversion efficiencies because of their favorable [110] crystallographic orientation.[5]

Surface modification with oxygen evolution catalysts (OEC) was also found to be an effective way to overcome the kinetic issues of water oxidation by hematite.[13,27] In addition, chemical modification by surface treatments was also reported to improve the electron donor density, flat band potential, and the optical absorption coefficient of hematite.[11,26] Doping of hematite with different elements such as Al,[19] Cd,[28] Mg,[29] Mo,[30] Si,[14,20] Sn,[12,31] Ti,[32] and Zn[26] has been shown to have a beneficial effect on the overall photoconversion efficiencies. For example, the performance enhancement of hematite resulting from Sn doping has been attributed to the similar ionic radius and electronegativity of Sn to that of $Fe^{3+}$ and to an improvement in the electronic properties of hematite by increasing the charge carrier density.[31] One such candidate that has not been explored in any depth for doping hematite is manganese even though manganese oxides have been extensively used as electrocatalysts for water oxidation and fuel cell applications[33−37] and manganese is the metal used in the natural water splitting site of photosynthesis.[38,39] Despite this, previous studies have found that surface treatment of hematite with $MnO_x$ was not encouraging, as it led to Fermi-level pinning, which caused a significant anodic shift and seemed to increase the recombination at the $\alpha$-$Fe_2O_3$−electrolyte interface.[40]

Here, we describe a strategy to enhance the PEC performance of hematite by doping with Mn. Mn is an attractive dopant in $Fe_2O_3$ because of the atomic radius and multivalent nature of Mn ions. Being next to Fe in the periodic table, the atomic radius of Mn is very close to that of Fe and therefore will not cause a significant distortion of the crystal structure of $Fe_2O_3$. Moreover, because Mn can exist as $Mn^{2+}$ and $Mn^{4+}$ ions, it is a potential p-type or n-type dopant for $Fe_2O_3$. Mn doping was also expected to generate energy states within the band gap of $Fe_2O_3$ and therefore could be beneficial in modulating the electrical conductivity.[41,42] We synthesized Mn-treated $Fe_2O_3$ photoanodes consisting of nanorods using a hydrothermal method, and, to the best of our knowledge, this is the first article describing the in situ growth of Mn-treated hematite nanostructures of this type and demonstrating their beneficial application for photoelectrochemical-driven water splitting.

## EXPERIMENTAL PROCEDURES

The pristine and Mn-treated hematite nanorod arrays were grown on a fluorine-treated tin oxide (FTO, Nippon Sheet Glass Co. Ltd, 15 ohm/sq, 1 × 2.5 $cm^2$) substrate. The hematite nanorods were prepared by a procedure modified from our previous work.[5] FTO-coated glass substrates were cleaned in the following sequence for 10 min each in an ultrasonication bath: (a) diluted deacon soap solution, (b) deionized (DI) water, (c) ethanol, (d) acetone, and (e) DI water. In short, a 10 mL aqueous solution containing 1.5 mmol of $FeCl_3 \cdot 6H_2O$ (Sigma-Aldrich) and 1.5 mmol of urea (Sigma-Aldrich) was transferred into a 20 mL Teflon-lined autoclave, and the substrates were placed with the FTO side facing the wall of the autoclave at an angle. The Mn-treated hematite nanorods were prepared using a similar method as the pristine hematite with 1, 2, 5, and 10% (by mole percent) $MnCl_2 \cdot 4H_2O$ (Sigma-Aldrich) added to the precursor solutions. After 10 h of reaction at 100 °C, a uniform layer of FeOOH film was formed on the FTO substrate. The substrates were thoroughly rinsed with DI water and annealed at 550 °C for 2 h to convert FeOOH to a hematite film. For PEC measurements, the samples were further annealed at 750 °C for 20 min.

**Characterization and Measurements.** X-ray diffraction patterns of pristine and Mn-treated hematite samples collected over a $2\theta$ range from 20 to 60° were carried out with a Shimadzu instrument (Lab X, XRD-6000) at an accelerating voltage 40 kV, a current of 30 mA, and a step size of 2°/min. The samples annealed at 550 °C were transferred ex situ to an ultrahigh vacuum (UHV) VG Escalab 220i-XL system equipped with a He ion discharge lamp (21.2 eV) for X-ray photoelectron spectroscopy (XPS) and ultraviolet photoelectron spectroscopy (UPS) characterization, respectively. The photoelectron signals were collected using a concentric hemispherical energy analyzer. A bias of −10 V was applied to collect the secondary electron cutoff. The ionization potential of the samples was measured by subtracting the width between the secondary cutoff and the valence band edge from the photon energy. The C 1s peak at 284.6 eV was used as the reference for any sample charging correction before the work function measurements, which was taken to be the difference between the secondary edges to the expected Fermi-level position.

Secondary ion mass spectrometry (SIMS) depth profiles were acquired using a TOFSIMS IV instrument from IONTOF (GmbH). A 3 keV $Ar^+$ ion beam was used for sputtering, and a pulsed 25 keV $Bi^+$ ion beam was used for analysis with detection of positive secondary ions. An electron flood gun was used for charge compensation.

The surface morphology of the samples was characterized by FESEM (JEOL, JSM-7600F, 5 kV), whereas ultraviolet−visible (UV−vis) absorption spectra of the pristine and Mn-treated hematite samples were obtained using a UV−vis−NIR spectrophotometer (PerkinElmer, Lambda 750S) equipped with an integrated sphere with a diameter of 60 mm. PEC measurements were performed using a CHI 660D working station (CH Instruments, Inc.) in a three-electrode electrochemical configuration with 1 M NaOH (pH 13.6) electrolyte. Platinum coil and Ag/AgCl were employed as the counter and reference electrodes, respectively. The working surface area was 0.12 $cm^2$. The light source was a 150 W xenon solar simulator (67005, Newport Corp.) equipped with a solar filter (KG 3), with a measured intensity equivalent to standard AM 1.5G sunlight (100 mW $cm^{-2}$) on the sample surface. Incident photon to current conversion efficiency (IPCE) characteristics were measured with a xenon light source (MAX-302, Asahi Spectra Co. Ltd.) coupled with a monochromator (CMS-100, Asahi Spectra Co. Ltd.) from 305 to 630 nm at a potential of 1.23 V versus RHE. A Si photodiode (Bentham, DH-Si) with known IPCE was used to calculate the IPCE of the pure hematite and Mn-treated hematite photoanodes. A source meter (Keithley Instruments Inc., model no. 2400) was used to measure the photocurrent of the Si diode. The working station (CHI 660D, CH Instruments, Inc.) was used to measure the photocurrent of the samples. Electrochemical impedance spectroscopy (EIS) measurements were carried out using an automated potentiostat (Methrohm-Autolab, AUT 83285) in a three-electrode electrochemical system. The reference and counter electrodes were the same as those for the PEC measurements. For Mott−Schottky plots, the EIS data were measured with a sinusoidal voltage perturbation of 10 mV in amplitude between 100 kHz to 100 Hz and were scanned from −1.0 to 1.0 V in the dark. A typical Mott−Schottky plot was extracted at 1 kHz. A gas chromatograph (GC) (Agilent 7890A) was employed to measure oxygen evolution under an

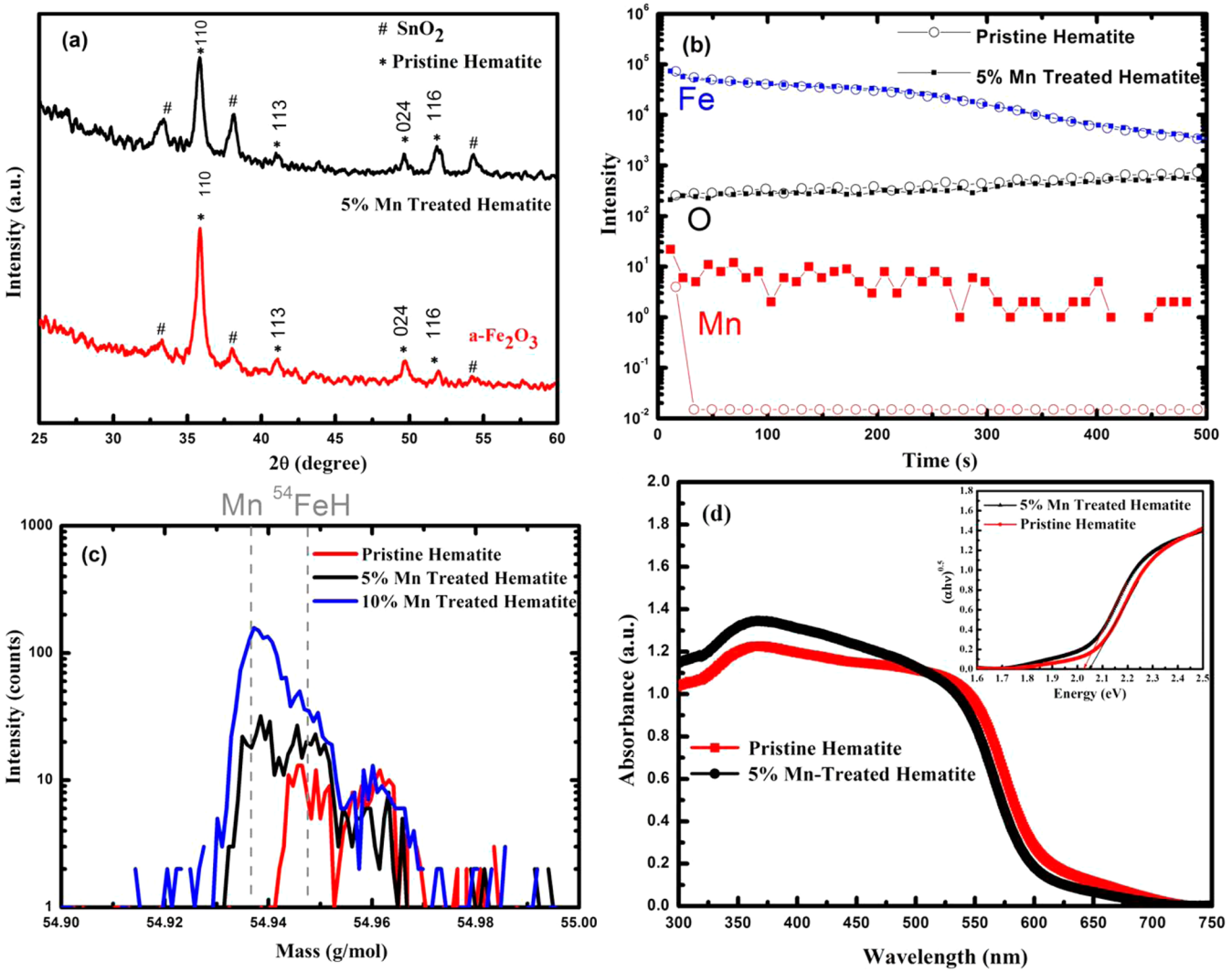


**Figure 1.** (a) XRD patterns of hematite ($\alpha$-$Fe_2O_3$) nanorod arrays on FTO without and with the Mn-treated sample after annealing at 550 °C for 2 h. The * denotes $\alpha$-$Fe_2O_3$ (JCPDS 33-0664), and # denotes $SnO_2$ (JCPDS 46-1088). (b) SIMS depth profile of both pristine and 5% Mn-treated $\alpha$-$Fe_2O_3$. (c) Intensity profile of the recorded secondary ions that have a mass near Mn. The shaded area shows the increase in the Mn contribution as the doping increased. (d) UV−vis absorption spectra of pristine hematite and 5% Mn-treated hematite; the inset shows the band gap extracted using Tauc's analysis.

intensity of 100 mW $cm^{-2}$ (AM 1.5G) (see above). The gas was manually presented to the GC by 0.5 mL injections. The potential of the working electrode was controlled at 1.23 V versus RHE in the three-electrode system. The active area of working electrode was 1.2 $cm^2$. Other conditions used were same as those for the PEC measurements. The 1 M NaOH electrolyte used for the PEC measurements was degassed by purging with $N_2$ gas for 10 min before measurements were recorded.

## RESULTS AND DISCUSSION

The XRD patterns of pristine hematite and Mn-treated hematite nanorods after 10 h of reaction and annealing at 550 °C for 2 h can be indexed to the characteristic peaks of $Fe_2O_3$ (JCPDS no. 003-0440) (Figure 1a). The strong (110) diffraction peak at $2\theta$ = 35.8° implies that the hematite nanorods grew preferentially in the [110] direction, as reported previously.[13] This is a preferred direction for charge transport because the conductivity in this (001) basal plane is 4 orders of magnitude higher than the orthogonal plane, which enhances the extent of the photo-oxidation process.[20] When Mn precursor was added with an initial molar ratio of Mn/Fe of 5%, no additional peak corresponding to the formation of manganese oxide in the XRD pattern was observed. Interestingly, neither a peak shift nor broadening of the XRD peaks, which is commonly associated with doping, were observed.[43] To check further for the incorporation of Mn into the hematite lattice, XPS and UPS analyses were performed. The XPS data obtained is shown in Figure S1. The presence of manganese was not detected, which could be explained by the actual amount of doping in the final sample being less than the amount added prior to the synthesis (5% by mol ratio), which is lower than the detection limit of XPS characterization (< 1%). Therefore, a more sensitive SIMS measurement was conducted on both the pristine and treated samples to confirm the presence of manganese (Figures 1b). Because the counts for Mn were relatively low, we examined the pristine and two differently treated hematite samples closely near the Mn mass (Figure 1c). Although the isotope mass of $^{54}$FeH is close to the Mn mass, our series of measurements show clearly that Mn is present and increased with the increasing concentration of the treatment. The low counts

measured on the intensity scale in Figure 1b,c also explain the lack of detection of manganese in the XPS measurements.

Although the presence of Mn is ∼1%, it can significantly change the electronic properties at the surface.[44,45] To check for the modulation of the electronic properties, surface work function measurements of the pristine and Mn-treated hematite were carried out using UPS. The work function of pristine hematite was 5.09 eV, whereas the Mn-treated sample has a smaller value of 4.79 eV (Figure S2). This indicates that Mn has a doping effect that shifts the Fermi level and changes the surface work function.[46] The shift in the Fermi level toward the conduction band facilitates the charge separation at the semiconductor−electrolyte interface by upward band bending toward the vacuum at the hematite surface.[46,47] UV−vis spectra of pristine hematite and Mn-treated hematite are shown in Figure 1d. The shape of the absorption curves and the band gaps extracted from Tauc's analysis are nearly the same (inset, Figure 1d). These samples show a similar optical band gap (2.05 and 2.07 eV), indicating that the doping level of Mn into the lattice of $Fe_2O_3$ is relatively low. The thickness of both the pristine and treated hematite samples remains the same (400 nm), as seen in Figure S3, and hence the optical absorption depth remain the same, as observed in the UV−vis spectra.

The top-view field-emission scanning electron microscopy (FESEM) images shown in Figure 2 reveal that pristine and

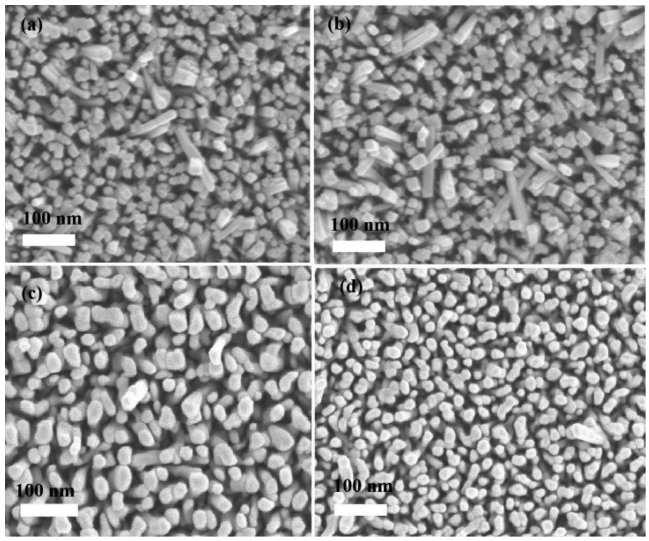


**Figure 2.** Top-view FESEM images of (a) pristine hematite after annealing at 550 °C, (b) 5% Mn-treated hematite after annealing at 550 °C (square cross-section), (c) pristine hematite after annealing at 750 °C, and (d) 5% Mn-treated hematite after annealing at 750 °C (circular cross-section).

Mn-treated hematite nanostructures grown on the FTO substrate exhibit a nanorod-like structure and that doping does not affect the growth process. These uniform nanorods have a square cross-section, a diameter that ranges from 50−60 nm, and a length that is ∼400 nm after annealing at 550 °C for 2 h (Figure 2a,b). After further annealing of these nanorods at 750 °C for 20 min, a slight increase in the diameter to ∼70 nm was observed, which is attributed to aggregation during high-temperature annealing (Figure 2c,d). However, some studies have shown that high-temperature annealing can induce the diffusion of Sn from the FTO layer into the hematite with a consequential increase in conductivity.[31]

Therefore, to achieve a higher efficiency, all of these parameters have to be considered and optimized. In this study, we found that annealing at 750 °C for 20 min is an optimized procedure based on the performance of the system.

Photocurrent−voltage measurements were carried out for pristine and Mn-treated hematite nanorods in 1 M NaOH electrolyte (pH 13.6) under simulated sunlight illumination at 100 mW $cm^{-2}$ from a 150 W xenon lamp coupled with an AM 1.5G filter, as seen in Figure 3a. All PEC measurements were performed with a three-electrode electrochemical configuration using an Ag/AgCl reference electrode and a Pt wire as the counter electrode. Photocurrent−voltage curves of pristine hematite with 5% initial Mn doping were found to give better performance compared to pristine samples (Figure 3a). The photocurrent−voltage plot of a higher (10%) Mn-treated sample is provided in the Supporting Information and yielded lower performance (Figure S4), and an initial Mn doping of 1 to 2% did not have any additional effect on the photocurrent (data not shown). The reduced photocurrent at high Mn doping could be due to an increase in the amount of electronic traps in the $Fe_2O_3$ band gap, which increase carrier recombination and reduce the overall photocurrent generated. The photocurrent density of 0.45 mA $cm^{-2}$ for the pristine hematite nanorods increased to 1.40 mA $cm^{-2}$ at 1.23 V versus RHE for the 5% Mn-treated sample. A plateau of about 2.4 mA $cm^{-2}$ for pristine hematite and 3.2 mA $cm^{-2}$ for 5% Mn-treated hematite from 1.6 to 1.8 V versus RHE was observed before the dark current rises. Thus, the increase in the photocurrent of the hematite photoanode with 5% Mn-treated hematite at 1.23 V versus RHE is more than 2-fold in comparison with the pristine hematite nanorods. Indeed the photocurrent density at 1.23 V with 5% Mn added is comparable with that obtained from hydrothermal-grown hematite nanorods decorated with the oxygen evolving catalyst $Co_3O_4$.[13] To understand the interplay between the photoactivity and the light absorption of the hematite nanorods, we measured their photoactivity as a function of the wavelength of the incident light. IPCE measurement is a well-established method to characterize the photoconversion efficiency of different photoanodes because it is independent of the light source and filter used in the measurement. IPCE measurements were performed on hematite with and without Mn-treated photoanodes at 1.23 V versus RHE (Figure 3b). IPCE can be expressed using the following equation[48]

$$\text{IPCE}\ (\%) = \left(\frac{1240 I_{\text{ph}}}{\lambda J_{\text{light}}}\right) 100 \qquad (1)$$

where $I_{\text{ph}}$ is the measured photocurrent density at a particular wavelength, $\lambda$ is the wavelength of incident light, and $J_{\text{light}}$ is the measured irradiance at a specific wavelength. In comparison to pristine hematite, Mn-treated hematite nanorods exhibit higher photoactivity over the entire UV−vis region. The IPCE drops to zero at wavelengths longer than 610 nm, which is consistent with the energetics of the hematite band gap.

Absorbed photon to current conversion (APCE) efficiency is shown in the inset of Figure 3b and was found to be higher for the Mn-treated sample, demonstrating its better collection and charge separation capability. The photocurrent density was calculated by integrating the IPCE spectra with a standard AM 1.5G (100 mW $cm^{-2}$) solar spectrum using the following equation[49]

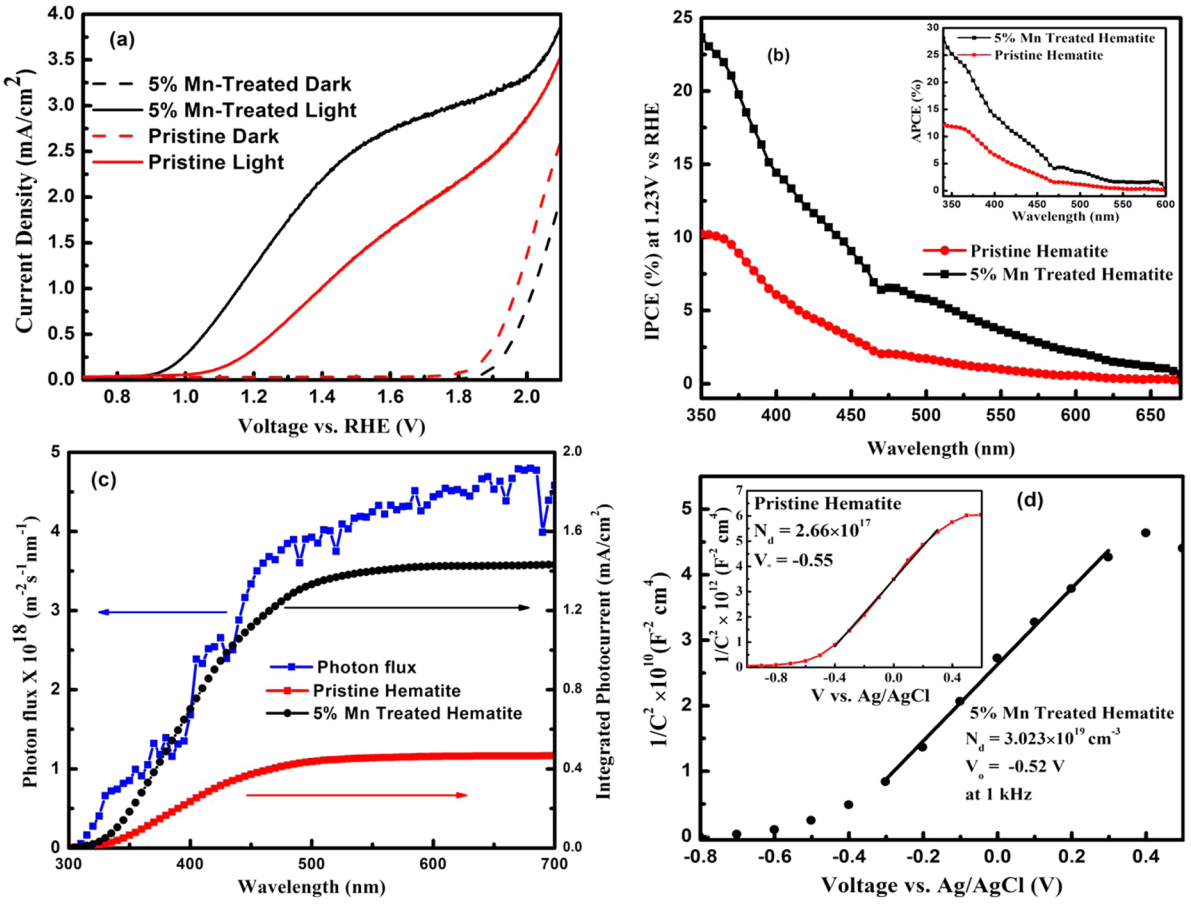


**Figure 3.** (a) Photocurrent−potential curve of the pristine hematite photoanode and 5% Mn-treated hematite measured under AM 1.5G illumination (100 mW cm$^{-2}$) in a 1 M NaOH electrolyte solution. (b) IPCE action spectrum of pristine hematite and 5% Mn-treated hematite collected at 1.23 V vs RHE; the inset shows APCE. (c) Integrated photocurrent based on the IPCE data (350−650 nm) collected at 1.23 V vs RHE; solar photon flux is shown as a reference. (d) Mott−Schottky plots of pristine (inset) and 5% Mn-treated hematite extracted from electrochemical impedance data measured at 1 kHz in the dark. Extracted donor densities ($N_d$) and flat band potentials ($V_0$) are shown in the figure.

$$I_{ph} = \int_{350}^{650} \frac{\lambda \mathrm{IPCE}(\lambda) J(\lambda)\, \mathrm{d}(\lambda)}{1240} \qquad (2)$$

where $J(\lambda)$ is the solar spectral irradiance at a particular wavelength ($\lambda$) and IPCE($\lambda$) is the obtained IPCE profile as a function of wavelengths ($\lambda$) at 1.23 V versus RHE. The calculated photocurrents were 0.41 and 1.4 mA cm$^{-2}$ for pristine and Mn-treated samples, respectively (Figure 3c), and concur well with the measured photocurrent densities at 1.23 V versus RHE. To understand the reason behind this increase in the photocurrent resulting from the presence of Mn, electrochemical impedance spectroscopy was performed because the optical absorption of both the pristine and treated hematite samples remained the same (Figure 1d).

Impedance measurements of the pristine and Mn-treated hematite samples annealed at 550 °C at a frequency of 1 and 10 kHz were performed under dark conditions. The flat band potential and donor densities of these samples were calculated from the slopes of Mott−Schottky plots using the equation[50,51]

$$\frac{1}{C^2} = \left(\frac{2}{\epsilon\varepsilon_0 N_d}\right)\left(V_A - V_0 - \frac{k_B T}{e}\right) \qquad (3)$$

where $C$ is the space charge layer capacitance, $e$ is the electron charge, $\varepsilon$ is the relative permittivity of hematite ($\varepsilon$ = 80),[52] $\varepsilon_0$ the permittivity of vacuum, $N_d$ is the donor density, $V_0$ is the flat band potential, and $V_A$ is the applied bias at the electrode. Hematite samples with and without 5% Mn-treated nanorods showed a positive slope in the Mott−Schottky plots, which is expected from a n-type semiconductor (Figures 3d and S5).[51]

The Mn-treated hematite sample exhibits a less acute slope and a reduced onset potential by 30 mV compared to pristine hematite. The donor density increases with Mn doping (Figure 3d). The calculated flat band potential and donor densities of the pristine hematite and 5% Mn-treated hematite nanorods were −0.55 V versus Ag/AgCl and 2.66 × 10$^{17}$ cm$^{-3}$ and −0.52 V versus Ag/AgCl and 3.02 × 10$^{19}$ cm$^{-3}$, respectively, at 1 kHz. Although the fact that Mott−Schottky is derived from a flat electrode model and may have errors in determining the absolute value of the donor density,[31] it is clear that Mn doping leads to a significant enhancement of the charge carrier density of hematite. An increased donor density is expected to shift the Fermi level of hematite toward the conduction band, which is also in agreement with the UPS results (Figure S2). However, a small discrepancy between the Mott−Schottky and UPS results arises from the fact that the former takes into account the influence of charge distribution resulting from the electrolyte, whereas UPS measures the real materials property. The increase in the photocurrent density for the treated hematite sample can be attributed to the increase in the charge carrier concentration, as calculated from the impedance measurements. Such an effect of modulating the charge carrier

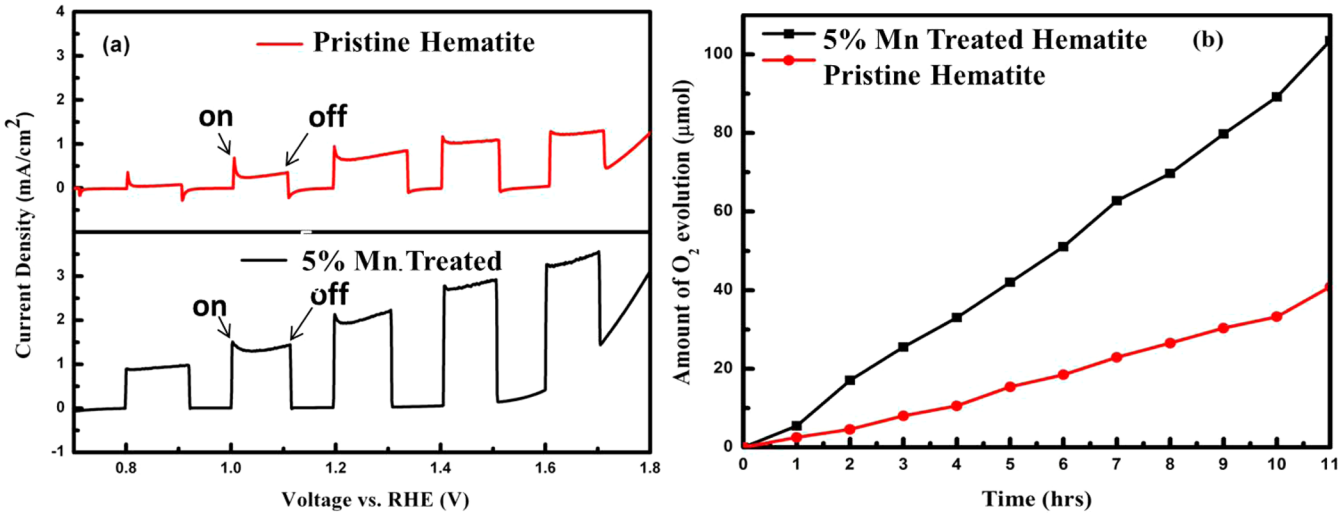


**Figure 4.** (a) Chopped photocurrent–potential curve of a pristine and 5% Mn-treated hematite photoanode. (b) Time progression of light-induced oxygen evolution of 5% Mn-treated hematite and pristine hematite photoanodes at an applied potential of 1.23 V vs RHE. Both sets of measurements were conducted under AM 1.5G (100 mW cm$^{-2}$) illumination in a 1 M NaOH electrolyte solution.

concentration by doping with other elements has also been observed previously.[31]

A low photocurrent onset and saturation potential is very important because it can reduce the voltage required to achieve the maximum photocurrent and thus increases the overall efficiency. The solar to chemical conversion efficiency ($\eta$) of nanorod photoanodes was calculated using eq 4.[53] (It should be noted that this equation is for two-electrode systems, and we assume that our three-electrode system generates the same current–voltage behavior. Moreover, the equation can also be used for qualitative comparison, as in our case.)

$$\eta = I_{ph}\left(\frac{1.23 - V}{J_{light}}\right) \quad (4)$$

where $V$ is the applied voltage versus RHE, $I_{ph}$ is the photocurrent density at the particular voltage, and $J_{light}$ is the irradiance intensity of 100 mW cm$^{-2}$ (AM 1.5G). The calculated solar to chemical conversion efficiency as a function of the applied bias is shown in Figure S5. The pristine hematite sample exhibits an optimal conversion efficiency of 0.24% at 1.15 versus RHE, and the Mn-treated hematite achieves a significantly higher efficiency of 0.95% at a low bias of 1.09 V versus RHE. The photoresponse with increasing bias voltage of both the pristine and Mn-treated hematite was measured with chopped illumination at 0.02 Hz under AM 1.5G solar irradiance and is shown in Figure 4a. The positive transients in photocurrent upon illumination represent the accumulation of holes at the electrode–electrolyte interface without injection into the electrolyte. Similarly, negative transients in photocurrent observed upon turning the light off reflect the back reaction of photoinduced electrons recombining with the accumulated holes. The current transients were found to disappear at high potentials, which indicates that the injection barrier does not impede the transfer of holes from the electrode to the electrolyte and therefore nearly all of the holes that reach the surface participate in the water oxidation reaction. Faradaic current is a steady-state current that occurs because of charge transfer without recombination (noncapacitive). At lower voltages, a mixture of both transient and faradaic currents was observed for the Mn-treated sample under illumination, whereas the pristine sample clearly demonstrated transient behavior. This difference is attributed to the accumulation of holes at semiconductor–electrolyte interface, as is commonly observed in pristine hematite samples.[54] This implies that for Mn-treated hematite sample most of the holes generated upon illumination contribute to water oxidation and indicates the suppression of electron–hole recombination.[54,55] Moreover, such a suppression in current transient behavior is usually observed when a redox reagent or hole scavenger are employed in the electrolyte solution.[54−56] Apparently the preparation method for generating nanostructured hematite has a direct effect in reducing the transient behavior, as has been observed in previous studies, and is further reflected in the Mn-treated samples investigated in this work.[55] When the light is switched off, a transient behavior is again observed for pristine hematite. As stated above, this is due to recombination of the excited electrons in the conduction band with the holes that are accumulated at the semiconductor–electrolyte interface.[55] This effect was reduced after Mn doping, possibly because the multivalent oxidation states of manganese leads to a low (O–Mn–O) energy barrier for hole transport.[41] This is also reflected in the APCE measurements (Figure 3b, inset), where the collection efficiency of the photoexcited charges increased by 100% (at $\lambda$ = 350 nm) for the Mn-treated samples. In addition, the current transients disappeared, and purely faradaic photocurrents were observed in the complete potential range in the pristine and 5% Mn-treated samples (Figure S8) after using a hole scavenger. This confirms that the injection barrier that was clearly observed in the 1 M NaOH electrolyte was removed by addition of 0.5 M $H_2O_2$.

To check the stability of the samples, photoresponse as a function of time was measured at 1.3 V versus RHE with chopped illumination under AM 1.5G solar irradiance up to 600 s, as shown in Figure S6. The overall photocurrent response with time was higher for the Mn-treated sample compared to the pristine hematite.

Oxygen evolution experiments were also conducted to confirm that the photocurrent generated is translated to $O_2$ production. As can be seen in Figure 4b, the rate of oxygen generation with the 5% Mn-treated hematite photoanode was


dx.doi.org/10.1021/am500643y | ACS Appl. Mater. Interfaces 2014, 6, 5852–5859

significantly larger than that of the pristine hematite. On the basis of the calculated faradaic efficiencies of 70.03 and 73.64% for 5% Mn-treated and pristine hematite, respectively, the amount of $O_2$ evolved was less than expected. This is probably due, in part, to gas leakage during the sampling and manual injection into the GC. Nevertheless, most of the photogenerated holes were consumed for oxygen production in our PEC system.

## CONCLUSIONS

We have demonstrated a solution-based method to synthesize Mn-treated hematite nanorods with improved water splitting activity compared to nontreated hematite nanorods. Systematic studies were performed to investigate the presence of Mn in the hematite nanostructures. Precursor doping with 5 mol % Mn was found to be optimum to enhance the photocurrent densities by 3-fold at 1.23 V versus RHE and also to reduce the onset potential by 30 mV compared to the pristine hematite. The enhancement in current density was attributed to an increase in the charge carrier density, as estimated by Mott–Schottky analysis. Chronoamperometry studies also showed that there is a decrease in transient currents for Mn-treated samples compared to pristine hematite, indicating the beneficial effects of Mn doping, which seems to be due to a suppression of electron–hole recombination and a reduction in the energy barrier for hole transport. This study confirms that Mn doping enhances the charge carriers and reduces the recombination losses, and it emphasizes that this treatment results in better PEC performance of $Fe_2O_3$ nanostructured photoanodes.

## ASSOCIATED CONTENT

### Supporting Information

XPS survey scans, UPS measurements, cross-section FESEM images, PEC curves, Mott–Schottky plots, photo conversion efficiency results of pristine and Mn-treated hematite. This material is available free of charge via the Internet at http://pubs.acs.org.

## AUTHOR INFORMATION

### Corresponding Authors

*E-mail: j.barber@imperial.ac.uk (J.B.).
*E-mail: lydiawong@ntu.edu.sg (L.H.W.).

### Notes

The authors declare no competing financial interest.

## ACKNOWLEDGMENTS

We acknowledge financial support from the Centre of Artificial Photosynthesis via the Solar Fuels Lab at NTU and Singapore National Research Foundation (NRF) through the Singapore–Berkeley Research Initiative for Sustainable Energy (SinBeRISE) CREATE Programme.

## REFERENCES

(1) Brillet, J.; Grätzel, M.; Sivula, K. Decoupling Feature Size and Functionality in Solution-Processed, Porous Hematite Electrodes for Solar Water Splitting. *Nano Lett.* **2010**, *10*, 4155–4160.

(2) Sivula, K.; Le Formal, F.; Grätzel, M. Solar Water Splitting: Progress Using Hematite ($\alpha$-$Fe_2O_3$) Photoelectrodes. *ChemSusChem* **2011**, *4*, 432–449.

(3) Sivula, K.; Zboril, R.; Le Formal, F.; Robert, R.; Weidenkaff, A.; Tucek, J.; Frydrych, J.; Grätzel, M. Photoelectrochemical Water Splitting with Mesoporous Hematite Prepared by a Solution-Based Colloidal Approach. *J. Am. Chem. Soc.* **2010**, *132*, 7436–7444.

(4) Wheeler, D. A.; Wang, G.; Ling, Y.; Li, Y.; Zhang, J. Z. Nanostructured Hematite: Synthesis, Characterization, Charge Carrier Dynamics, and Photoelectrochemical Properties. *Energy Environ. Sci.* **2012**, *5*, 6682–6702.

(5) Mulmudi, H. K.; Mathews, N.; Dou, X. C.; Xi, L. F.; Pramana, S. S.; Lam, Y. M.; Mhaisalkar, S. G. Controlled Growth of Hematite ($\alpha$-$Fe_2O_3$) Nanorod Array on Fluorine Doped Tin Oxide: Synthesis and Photoelectrochemical Properties. *Electrochem. Commun.* **2011**, *13*, 951–954.

(6) Murphy, A. B.; Barnes, P. R. F.; Randeniya, L. K.; Plumb, I. C.; Grey, I. E.; Horne, M. D.; Glasscock, J. A. Efficiency of Solar Water Splitting Using Semiconductor Electrodes. *Int. J. Hydrogen Energy* **2006**, *31*, 1999–2017.

(7) Young, K. M. H.; Klahr, B. M.; Zandi, O.; Hamann, T. W. Photocatalytic Water Oxidation with Hematite Electrodes. *Catal. Sci. Technol.* **2013**, *3*, 1660–1671.

(8) Bora, D. K.; Braun, A.; Constable, E. C. "In Rust We Trust". Hematite – the Prospective Inorganic Backbone for Artificial Photosynthesis. *Energy Environ. Sci.* **2013**, *6*, 407–425.

(9) Barroso, M.; Pendlebury, S. R.; Cowan, A. J.; Durrant, J. R. Charge Carrier Trapping, Recombination and Transfer in Hematite ($\alpha$-$Fe_2O_3$) Water Splitting Photoanodes. *Chem. Sci.* **2013**, *4*, 2724–2734.

(10) Lin, Y.; Yuan, G.; Sheehan, S.; Zhou, S.; Wang, D. Hematite-Based Solar Water Splitting: Challenges and Opportunities. *Energy Environ. Sci.* **2011**, *4*, 4862–4869.

(11) Xi, L.; Chiam, S. Y.; Mak, W. F.; Tran, P. D.; Barber, J.; Loo, S. C. J.; Wong, L. H. A Novel Strategy for Surface Treatment on Hematite Photoanode for Efficient Water Oxidation. *Chem. Sci.* **2013**, *4*, 164–169.

(12) Cai, J.; Li, S.; Li, Z.; Wang, J.; Ren, Y.; Qin, G. Electrodeposition of Sn-Doped Hollow $\alpha$-$Fe_2O_3$ Nanostructures for Photoelectrochemical Water Splitting. *J. Alloys Compd.* **2013**, *574*, 421–426.

(13) Xi, L.; Tran, P. D.; Chiam, S. Y.; Bassi, P. S.; Mak, W. F.; Mulmudi, H. K.; Batabyal, S. K.; Barber, J.; Loo, J. S. C.; Wong, L. H. $Co_3O_4$-Decorated Hematite Nanorods as an Effective Photoanode for Solar Water Oxidation. *J. Phys. Chem. C* **2012**, *116*, 13884–13889.

(14) Liu, J.; Liang, C.; Zhang, H.; Zhang, S.; Tian, Z. Silicon-Doped Hematite Nanosheets with Superlattice Structure. *Chem. Commun.* **2011**, *47*, 8040–8042.

(15) Yang, Y.; Ma, H.; Zhuang, J.; Wang, X. Morphology-Controlled Synthesis of Hematite Nanocrystals and Their Facet Effects on Gas-Sensing Properties. *Inorg. Chem.* **2011**, *50*, 10143–10151.

(16) Bassi, P. S.; Gurudayal; Wong, L. H.; Barber, J. Iron Based Photoanodes for Solar Fuel Production *Phys. Chem. Chem. Phys.* [Online early access]. DOI: 10.1039/C3CP55174A. Published Online: Jan 22, **2014**.

(17) Kumar, P.; Sharma, P.; Shrivastav, R.; Dass, S.; Satsangi, V. R. Electrodeposited Zirconium-Doped $\alpha$-$Fe_2O_3$ Thin Film for Photoelectrochemical Water Splitting. *Int. J. Hydrogen Energy* **2011**, *36*, 2777–2784.

(18) Duret, A.; Grätzel, M. Visible Light-Induced Water Oxidation on Mesoscopic $\alpha$-$Fe_2O_3$ Films Made by Ultrasonic Spray Pyrolysis. *J. Phys. Chem. B* **2005**, *109*, 17184–17191.

(19) Le Formal, F.; Tétreault, N.; Cornuz, M.; Moehl, T.; Grätzel, M.; Sivula, K. Passivating Surface States on Water Splitting Hematite Photoanodes with Alumina Overlayers. *Chem. Sci.* **2011**, *2*, 737–743.

(20) Kay, A.; Cesar, I.; Grätzel, M. New Benchmark for Water Photooxidation by Nanostructured $\alpha$-$Fe_2O_3$ Films. *J. Am. Chem. Soc.* **2006**, *128*, 15714–15721.

(21) Vayssieres, L.; Sathe, C.; Butorin, S. M.; Shuh, D. K.; Nordgren, J.; Guo, J. One-Dimensional Quantum-Confinement Effect in $\alpha$-$Fe_2O_3$ Ultrafine Nanorod Arrays. *Adv. Mater.* **2005**, *17*, 2320–2323.

(22) Lindgren, T.; Wang, H.; Beermann, N.; Vayssieres, L.; Hagfeldt, A.; Lindquist, S. E. Aqueous Photoelectrochemistry of Hematite Nanorod Array. *Sol. Energy Mater. Sol. Cells* **2002**, *71*, 231–243.

(23) Beermann, N.; Vayssieres, L.; Lindquist, S. E.; Hagfeldt, A. Photoelectrochemical Studies of Oriented Nanorod Thin Films of Hematite. *J. Electrochem. Soc.* **2000**, *147*, 2456–2461.

(24) Vincent, T.; Gross, M.; Dotan, H.; Rothschild, A. Thermally Oxidized Iron Oxide Nanoarchitectures for Hydrogen Production by Solar-Induced Water Splitting. *Int. J. Hydrogen Energy* **2012**, *37*, 8102−8109.
(25) Zeng, S.; Tang, K.; Li, T.; Liang, Z.; Wang, D.; Wang, Y.; Qi, Y.; Zhou, W. Facile Route for the Fabrication of Porous Hematite Nanoflowers: Its Synthesis, Growth Mechanism, Application in the Lithium Ion Battery, and Magnetic and Photocatalytic Properties. *J. Phys. Chem. C* **2008**, *112*, 4836−4843.
(26) Xi, L.; Bassi, P. S.; Chiam, S. Y.; Mak, W. F.; Tran, P. D.; Barber, J.; Chye Loo, J. S.; Wong, L. H. Surface Treatment of Hematite Photoanodes with Zinc Acetate for Water Oxidation. *Nanoscale* **2012**, *4*, 4430−4433.
(27) Warren, S. C.; Voïtchovsky, K.; Dotan, H.; Leroy, C. M.; Cornuz, M.; Stellacci, F.; Hébert, C.; Rothschild, A.; Grätzel, M. Identifying Champion Nanostructures for Solar Water-Splitting. *Nat. Mater.* **2013**, *12*, 842−849.
(28) Bak, A.; Choi, W.; Park, H. Enhancing the Photoelectrochemical Performance of Hematite ($\alpha$-$Fe_2O_3$) Electrodes by Cadmium Incorporation. *Appl. Catal., B* **2011**, *110*, 207−215.
(29) Mohapatra, M.; Padhi, T.; Anand, S.; Mishra, B. K. CTAB Mediated Mg-Doped Nano $Fe_2O_3$: Synthesis, Characterization, and Fluoride Adsorption Behavior. *Desalin. Water Treat.* **2012**, *50*, 376−386.
(30) Kleiman-Shwarsctein, A.; Hu, Y. S.; Forman, A. J.; Stucky, G. D.; McFarland, E. W. Electrodeposition of $\alpha$-$Fe_2O_3$ Doped with Mo or Cr as Photoanodes for Photocatalytic Water Splitting. *J. Phys. Chem. C* **2008**, *112*, 15900−15907.
(31) Ling, Y.; Wang, G.; Wheeler, D. A.; Zhang, J. Z.; Li, Y. Sn-Doped Hematite Nanostructures for Photoelectrochemical Water Splitting. *Nano Lett.* **2011**, *11*, 2119−2125.
(32) Zhang, P.; Kleiman-Shwarsctein, A.; Hu, Y. S.; Lefton, J.; Sharma, S.; Forman, A. J.; McFarland, E. Oriented Ti Doped Hematite Thin Film as Active Photoanodes Synthesized by Facile Apcvd. *Energy Environ. Sci.* **2011**, *4*, 1020−1028.
(33) Roche, I.; Chaînet, E.; Chatenet, M.; Vondrák, J. Carbon-Supported Manganese Oxide Nanoparticles as Electrocatalysts for the Oxygen Reduction Reaction (ORR) in Alkaline Medium: Physical Characterizations and ORR Mechanism. *J. Phys. Chem. C* **2007**, *111*, 1434−1443.
(34) El-Deab, M. S.; Ohsaka, T. Manganese Oxide Nanoparticles Electrodeposited on Platinum Are Superior to Platinum for Oxygen Reduction. *Angew. Chem., Int. Ed.* **2006**, *45*, 5963−5966.
(35) Feng, R. X.; Dong, H.; Wang, Y. D.; Ai, X. P.; Cao, Y. L.; Yang, H. X. A Simple and High Efficient Direct Borohydride Fuel Cell with $MnO_2$-Catalyzed Cathode. *Electrochem. Commun.* **2005**, *7*, 449−452.
(36) Samant, P. V.; Fernandes, J. B. Nickel-Modified Manganese Oxide as an Active Electrocatalyst for Oxidation of Methanol in Fuel Cells. *J. Power Sources* **1999**, *79*, 114−118.
(37) Vondrák, J.; Sedlavíková, M.; Novák, V. Electrocatalysts Based on Carbon-Manganese Oxide for Alkaline Fuel Cell Cathodes. *J. New Mater. Electrochem. Syst.* **1998**, *1*, 25−30.
(38) Ferreira, K. N.; Iverson, T. M.; Maghlaoui, K.; Barber, J.; Iwata, S. Architecture of the Photosynthetic Oxygen-Evolving Center. *Science* **2004**, *303*, 1831−1838.
(39) Barber, J.; Murray, J. W. The Structure of the $Mn_4Ca^{2+}$ Cluster of Photosystem II and Its Protein Environment as Revealed by X-ray Crystallography. *Philos. Trans. R. Soc., B* **2008**, *363*, 1129−1137.
(40) Yang, X.; Du, C.; Liu, R.; Xie, J.; Wang, D. Balancing Photovoltage Generation and Charge-Transfer Enhancement for Catalyst-Decorated Photoelectrochemical Water Splitting: A Case Study of the Hematite/$MnO_x$ Combination. *J. Catal.* **2013**, *304*, 86−91.
(41) Liao, P.; Carter, E. A. Hole Transport in Pure and Doped Hematite. *J. Appl. Phys.* **2012**, *112*, 013701-1−013701-13.
(42) Balko, B. A.; Clarkson, K. M. The Effect of Doping with Ti(IV) and Sn(IV) on Oxygen Reduction at Hematite Electrodes. *J. Electrochem. Soc.* **2001**, *148*, E85−E91.
(43) Prabhakar, R. R.; Mathews, N.; Jinesh, K. B.; Karthik, K. R. G.; Pramana, S. S.; Varghese, B.; Sow, C. H.; Mhaisalkar, S. Efficient Multispectral Photodetection Using Mn Doped ZnO Nanowires. *J. Mater. Chem.* **2012**, *22*, 9678−9683.
(44) Zhang, H.; Chen, G.; Bahnemann, D. W. Photoelectrocatalytic Materials for Environmental Applications. *J. Mater. Chem.* **2009**, *19*, 5089−5121.
(45) Zhang, X.; Zhang, L. Electronic and Band Structure Tuning of Ternary Semiconductor Photocatalysts by Self Doping: The Case of BiOI. *J. Phys. Chem. C* **2010**, *114*, 18198−18206.
(46) Gassenbauer, Y.; Klein, A. Electronic and Chemical Properties of Tin-Doped Indium Oxide (ITO) Surfaces and ITO/ZnPc Interfaces Studied in-Situ by Photoelectron Spectroscopy. *J. Phys. Chem. B* **2006**, *110*, 4793−4801.
(47) Greiner, M. T.; Lu, Z. H. Thin-Film Metal Oxides in Organic Semiconductor Devices: Their Electronic Structures, Work Functions and Interfaces. *NPG Asia Mater.* **2013**, *5*.
(48) Yang, X.; Lian, X.; Liu, S.; Tian, J.; Jiang, C.; Wang, G.; Chen, J.; Wang, R. Investigation of Enhanced Photoelectrochemical Property of Cerium Doped Hematite Film Prepared by Sol-Gel Route. *Int. J. Electrochem. Sci.* **2013**, *8*, 3721−3730.
(49) Tsui, L. K.; Zangari, G. The Influence of Morphology of Electrodeposited $Cu_2O$ and $Fe_2O_3$ on the Conversion Efficiency of $TiO_2$ Nanotube Photoelectrochemical Solar Cells. *Electrochim. Acta* **2013**, *100*, 220−225.
(50) Klahr, B.; Gimenez, S.; Fabregat-Santiago, F.; Bisquert, J.; Hamann, T. W. Photoelectrochemical and Impedance Spectroscopic Investigation of Water Oxidation with "Co-Pi"-Coated Hematite Electrodes. *J. Am. Chem. Soc.* **2012**, *134*, 16693−16700.
(51) Shimizu, K.; Lasia, A.; Boily, J. F. Electrochemical Impedance Study of the Hematite/Water Interface. *Langmuir* **2012**, *28*, 7914−7920.
(52) Kennedy, J. H.; Frese, K. W., Jr. Flatband Potential and Donor Density of Polycrystalline Alpha-$Fe_2O_3$ Determined from Mott−Schottky Plots. *J. Electrochem. Soc.* **1978**, *125*, 723−726.
(53) Mao, A.; Kim, J. K.; Shin, K.; Wang, D. H.; Yoo, P. J.; Han, G. Y.; Park, J. H. Hematite Modified Tungsten Trioxide Nanoparticle Photoanode for Solar Water Oxidation. *J. Power Sources* **2012**, *210*, 32−37.
(54) Dotan, H.; Sivula, K.; Gratzel, M.; Rothschild, A.; Warren, S. C. Probing the Photoelectrochemical Properties of Hematite ($\alpha$-$Fe_2O_3$) Electrodes Using Hydrogen Peroxide as a Hole Scavenger. *Energy Environ. Sci.* **2011**, *4*, 958−964.
(55) Iwanski, P.; Curran, J. S.; Gissler, W.; Memming, R. The Photoelectrochemical Behavior of Feric Oxide in the Presence of Redox Reagents. *J. Electrochem. Soc.* **1981**, *128*, 2128−2133.
(56) Le Formal, F.; Sivula, K.; Grätzel, M. The Transient Photocurrent and Photovoltage Behavior of a Hematite Photoanode under Working Conditions and the Influence of Surface Treatments. *J. Phys. Chem. C* **2012**, *116*, 26707−26720.